

# Hole spin dynamics and valence-band spin excitations in two-dimensional hole systems

## Feature Article

T. Korn\* and C. Schüller

Institut für Experimentelle und Angewandte Physik, Universität Regensburg, 93040 Regensburg, Germany

Received 10 September 2013, revised 30 October 2013, accepted 30 October 2013

Published online 6 December 2013

**Keywords** electronic excitations, inelastic light scattering, spin dynamics, two-dimensional hole systems

\* Corresponding author: e-mail tobias.korn@physik.uni-r.de, Phone: +49 941 9432055, Fax: +49 941 9434226



This is an open access article under the terms of the Creative Commons Attribution License, which permits use, distribution and reproduction in any medium, provided the original work is properly cited.

In recent years, the spin dynamics and spin–orbit interaction in GaAs-based two-dimensional hole systems (2DHS) have created a lot of attention. This is due to the complex structure of the valence band, with its p-like character, which leads to strong spin–orbit coupling. In this paper, we review our recent studies on hole spin dynamics and valence-band spin excitations in GaAs-based, p-modulation-doped quantum wells (QWs). In 2DHS with low carrier concentration, we demonstrate that maximizing the heavy-hole–light-hole band splitting by changing the QW width leads to long hole spin dephasing times at low temperatures. Different mechanisms for initializing a resident hole spin polarization by optical excitation are presented. To accurately determine hole spin dynamics parameters, the

resonant spin amplification technique is utilized. The strong anisotropy of the hole  $g$  factor, and electrical  $g$  factor control are investigated, using this technique. In highly doped 2DHS, we use resonant inelastic light scattering (RILS) to study the spin splitting of the valence band. We observe a low-energy spin-density excitation (SDE), which is a measure of the spin splitting of the hole ground state. By varying the laser energy in the RILS experiment, we can resonantly probe the  $k$  dependence of the spin splitting. The spectral shape of the SDE depends on the orientation of the light polarizations relative to the crystal axes and reflects the in-plane anisotropy of the valence-band spin splitting.

**1 Introduction** The spin dynamics and spin–orbit coupling in semiconductor heterostructures have been investigated intensely in recent years, in part due to possible applications in semiconductor spintronics [1–3]. A lot of studies have focussed on direct-gap semiconductors, such as the GaAs/AlGaAs material system, as it gives a lot of flexibility in the design and symmetry of heterostructures, and high-quality growth of such structures via molecular beam epitaxy (MBE) is a mature technique. They are well-suited as model systems, as optical spectroscopy techniques can be used to study the spin dynamics [4]. While the majority of experimental and theoretical investigations deal with the spin dynamics of electrons in the conduction band, interest in valence-band spin dynamics has increased in recent years, driven by the availability of high-mobility samples [5] and prediction of large spin-Hall effects in GaAs-based two-dimensional hole systems (2DHS) [6]. Due to the p-like

character of the valence band in GaAs-based heterostructures, as compared to the s-like character of the conduction band, spin–orbit coupling in the valence band is in most cases much stronger than in the conduction band. Additionally, the valence band structure is more complex, with heavy-hole (HH), light-hole (LH), and split-off hole bands. In GaAs bulk, HH and LH bands are degenerate at  $k = 0$ . As these bands have different angular momentum, any momentum scattering can lead to a change of hole spin orientation. Therefore, hole spin dephasing in GaAs bulk occurs on the order of the momentum scattering time of about 100 fs [7]. The HH–LH degeneracy is lifted in quantum wells (QWs), leading to an increase of the hole spin dephasing time [8]. However, due to valence-band mixing, the character of the bands is not well-defined for  $k > 0$ , so that long hole spin dephasing times can only be expected for low-doped 2DHS at low temperatures, where the hole wave vector is close to zero. Initial studies

**Table 1** Properties of the samples used for hole spin dynamics studies. Density and mobility were determined from magnetotransport measurements at 1.3 K.

#	QW width (nm)	hole density $p$ ( $10^{11} \text{ cm}^{-2}$ )	hole mobility $\mu$ ( $10^5 \text{ cm}^2 \text{ V}^{-1} \text{ s}^{-1}$ )	electron $g$ factor $ g_e $
A	15	0.90	5.0	0.280
B	9	1.03	3.6	0.133
C	7.5	1.10	5.3	0.106
D	4	1.10	0.13	0.266

of long-lived hole spin dynamics [9] and hole spin precession [10] were performed on n-doped QWs, using time-resolved photoluminescence to determine the spin polarization of the optically oriented holes. Several years later, time-resolved Kerr rotation (TRKR) was used to observe, both, electron and hole spin dynamics in p-doped QWs [11].

For  $k > 0$ , the spin-orbit interaction leads to a  $k$ -dependent valence-band spin splitting even in the absence of an external magnetic field. This spin splitting originates either from bulk inversion asymmetry (Dresselhaus field), or from a growth-axis asymmetry of a heterostructure (Rashba field), which may be caused, e.g., by asymmetric modulation doping or a growth-axis electric field. In single-side-doped 2DHS, the Rashba contribution is often much larger than the Dresselhaus contribution [12]. To directly measure the spin splitting in the *conduction* band, Jusserand et al. utilized resonant inelastic light scattering (RILS) [13].

Here, we will review our recent results on hole spin dynamics in p-doped QWs. We investigate, both, the hole spin dynamics in low-doped 2DHS, and valence-band spin excitations in highly doped 2DHS. We show a pronounced increase of the hole spin dephasing time with increasing HH-LH splitting and demonstrate different initialization mechanisms for a resident hole spin polarization. In samples with long hole spin dephasing times, we use the resonant spin amplification (RSA) technique to measure hole spin dynamics in weak magnetic fields. Additionally, we investigate the anisotropy of the hole  $g$  factor, demonstrate electrical  $g$  factor control and study hole spin dynamics in tilted magnetic fields. By using RILS, we are able to directly observe a spin-density excitation (SDE), whose energy corresponds to the valence-band spin splitting. By changing the excitation energy and the light polarization relative to the crystal axes, we show the dependence of the spin splitting on the magnitude and crystallographic orientation of the hole wave vector.

## 2 Hole spin dynamics

**2.1 Samples and experiment** The samples used in the hole spin dynamics experiments are single-side p-modulation-doped GaAs/Al<sub>0.3</sub>Ga<sub>0.7</sub>As QWs, containing a 2DHS. All samples were grown by MBE. Their properties are given in Table 1. For measurements in transmission, some samples were thinned. For this, the samples were first glued onto a sapphire substrate with optically transparent glue, then the semiconductor substrate was removed by grinding and

selective wet etching. The samples contain a short-period GaAs/AlGaAs superlattice, which serves as an etch stop, leaving only the MBE-grown layers. Additionally, a semi-transparent top gate was prepared on some samples. For this, a thin NiCr layer was thermally evaporated on top of the sample. The 2DHS was contacted from the top by alloying indium contacts.

Two different cryostat systems were used for the experiments. Measurements below liquid-helium temperature were performed in an optical cryostat with <sup>3</sup>He insert, allowing us to lower the sample temperatures below 400 mK. In this cryostat, the samples are cooled by cold <sup>3</sup>He gas. Magnetic fields of up to 11.5 T can be applied. The samples are mounted on a sample rod within the cryostat and can be rotated manually with respect to the magnetic field orientation. The rotation angle is measured with high precision using a laser pointer mounted to the sample rod. For some of these measurements, thinned samples were used and the experiment was performed in transmission (time-resolved Faraday rotation, TRFR) to limit the amount of absorbed laser power. Additionally, for measurements performed in transmission geometry, the sample can be rotated without any changes to the optical beam path. Measurements above liquid-helium temperature were performed in a helium-flow cryostat, in which the samples are mounted on the cold finger of the cryostat in vacuum.

Pulsed Ti-sapphire laser systems, generating pulses with length between 600 fs and 2 ps, and corresponding spectral width from 1 to 4 meV, were used for the time-resolved measurements. The repetition rate of the laser systems is 80 MHz, corresponding to a time delay of 12.5 ns between subsequent pulses. The laser pulses are split into a circularly polarized pump beam and a linearly polarized probe beam by a beam splitter. A mechanical delay line is used to create a variable time delay between pump and probe. Both beams are focused to a diameter of about 80  $\mu\text{m}$  on the sample using an achromat.

In the TRKR and RSA experiments, the circularly polarized pump beam is generating electron-hole pairs in the QW, with spins aligned parallel or antiparallel to the beam direction, i.e., the QW normal, depending on the helicity of the light. In the TRKR measurements, the spin polarization created perpendicular to the sample plane by the pump beam is probed by the time-delayed probe beam via the Kerr effect: the axis of linear polarization of the probe beam is rotated by a small angle, which is proportional to the out-of-plane component of the spin polarization [14, 15]. This small angle is detected using an optical bridge. A lock-in scheme is used to increase sensitivity. The RSA technique is based on the interference of spin polarizations created in a sample by subsequent pump pulses. It requires that the spin dephasing time is comparable to the time delay between pump pulses. For certain magnetic fields applied in the sample plane, the optically oriented spin polarization precesses by an integer multiple of  $2\pi$  in the time window between subsequent pump pulses, so that constructive interference occurs. This leads to pronounced maxima in the Faraday or Kerr rotation angle, measured for a fixed time delay as a function of the applied

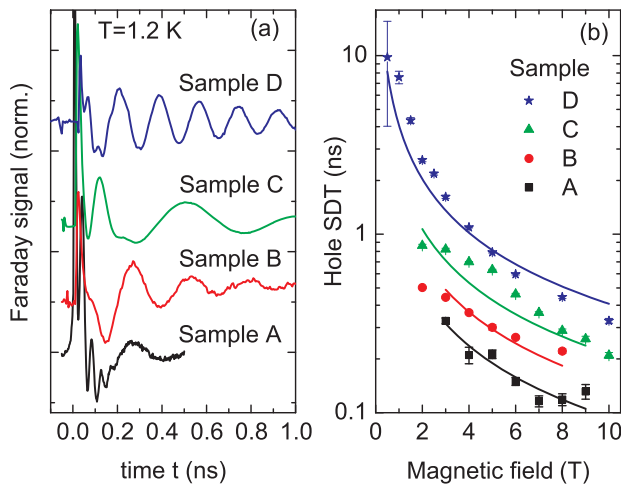


**Figure 1** (a) TRFR traces for samples A–D at 1.2 K. A 6 T in-plane magnetic field was applied during the measurements. (b) Hole SDTs for samples A–D as a function of magnetic field. The lines represent fits of a  $1/B$  dependence. Reprinted with permission from Ref. [17].

magnetic field. In our RSA measurements, the time delay is chosen to probe the spin polarization remaining within the sample 100 ps before the arrival of a pump pulse.

## 2.2 Optimizing sample design for long-lived hole spin dynamics

First, we discuss the optimal sample design for studying long-lived spin dynamics. As discussed above, a large splitting between the HH and LH bands at  $k = 0$  is necessary to create a well-defined HH state, which does not have a significant LH band admixture. The splitting between the valence bands in a QW arises due to the different effective masses of light and heavy holes and the quantization of the growth-axis momentum. It increases with decreasing QW width and reaches a maximum at a thickness of about 4 nm. For thinner QWs, the splitting decreases again due to penetration of the hole wave functions into the barrier material [16]. The effects of the changing HH–LH-splitting are directly observable in spin dynamics measurements, performed on a series of samples with different QW width: Fig. 1a shows TRFR traces measured on four different samples. All measurements were performed at a nominal sample temperature of 1.2 K, with an applied in-plane magnetic field of 6 T. In each TRFR trace, we see a maximum signal for  $t = 0$ , corresponding to the arrival of the pump pulse and optical orientation of electron–hole pairs. The Faraday signal then shows a superposition of two damped oscillations with different frequencies and damping constants. The fast oscillation at small  $t$  can be attributed to electron spin precession, as the  $g$  factor we extract from the data (see Table 1) is in good agreement with values reported for QWs of corresponding width [18, 19]. We note that the decay of this fast oscillation is not due to electron spin dephasing, but due to photocarrier recombination, which occurs on the 50–100 ps timescale in our samples at low temperatures [20]. Since the QWs are p-doped, electron spin dynamics can only be observed during the photocarrier lifetime. The slow oscil-

lation is due to hole spin precession, as the holes have a  $g$  factor, which is close to zero for in-plane orientation of the magnetic field [10, 21]. As this slow precession persists for times exceeding the photocarrier lifetime, it indicates that spin polarization is transferred to resident holes. The transfer mechanism will be discussed below. We clearly see that the decay of the hole spin precession becomes slower as the QW width is decreased. The spin dynamics parameters are extracted from the TRFR traces by fitting the sum of two damped cosine functions to the data. Figure 1b shows the hole spin dephasing time (SDT) as a function of the applied in-plane magnetic field for all the investigated samples. We note that the maximum hole SDT is observed in the 4 nm wide QW, and that for all samples, there is a pronounced decrease of the hole SDT with increasing magnetic field. This decrease is due to the inhomogeneous broadening  $\Delta g_h^*$  of hole  $g$  factors in our samples. At low temperatures, the resident holes in our QW are localized at QW thickness fluctuations, which are also referred to as natural quantum dots (QDs) [22]. They typically have lateral dimensions of 50–100 nm [23], significantly larger than self-assembled (In,Ga)As/GaAs QDs. In contrast to self-assembled QDs, there is no large inhomogeneous broadening due to local strain or changes of the material composition in natural QDs. Nevertheless, the local environment is slightly different for each localization center, and this leads to small differences of the hole  $g$  factor. For free carriers, these fluctuations are averaged out, and  $g$  factor broadening can be neglected even for two-dimensional electron systems (2DES) with large SDT [24]. As we study the spin dynamics of an ensemble of localized holes, we measure the ensemble hole SDT (this SDT is commonly referred to as  $T_2^*$ ). In an applied magnetic field, holes with different  $g$  factors will precess at different frequencies, leading to a (reversible) dephasing of the ensemble. In self-assembled QDs, this effect is very pronounced due to the large inhomogeneous broadening, so that techniques like spin mode locking have to be employed to study the spin dynamics of the ensemble [25].  $T_2^*$  is, in first approximation, given by [26]

$$T_2^* = \left( \frac{1}{T_2} + \frac{\Delta g_h^* \mu_B B}{\hbar} \right)^{-1}, \quad (1)$$

if  $\Delta g_h^*$  is considered as the only source of inhomogeneity. Here,  $T_2$  is the hole SDT in the absence of inhomogeneous broadening. We note that for the lowest magnetic field applied in this measurement series, the ensemble hole SDT in sample D is about 10 ns and thus exceeds the accessible time window of the TRFR experiment. Equation (1) indicates that the effect of inhomogeneous broadening is suppressed at low magnetic fields, so that low-field measurements are desirable to accurately determine  $T_2$ . This field regime is accessible in the RSA measurements, which will be discussed below.

## 2.3 Initialization of a hole spin polarization

Next, we discuss the initialization of a hole spin polarization by optical orientation. In 2DES or n-bulk GaAs,

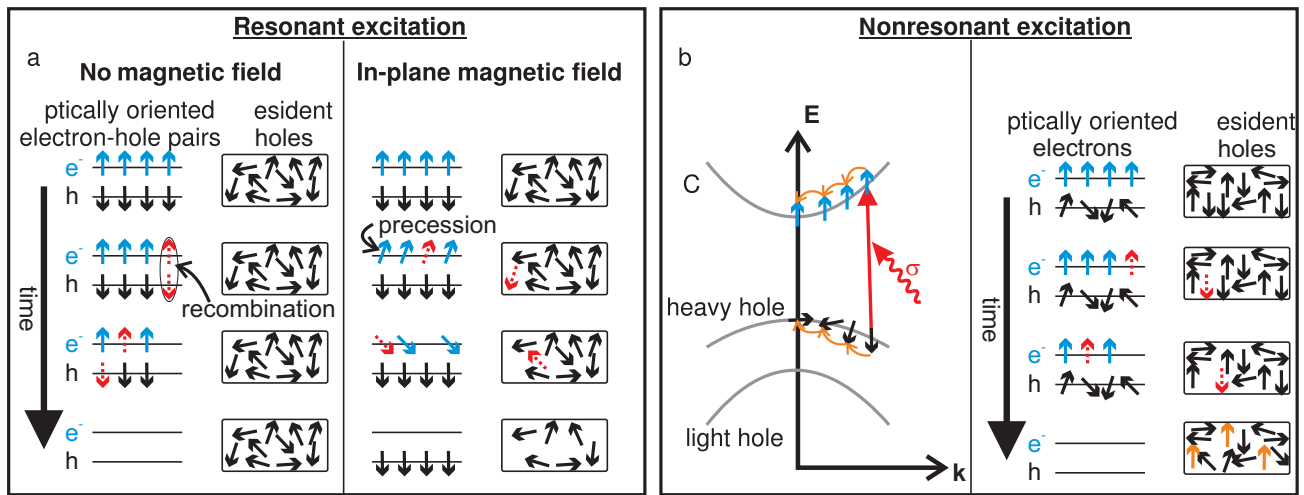


**Figure 2** (a) Diagram of the combined spin and recombination dynamics for resonant excitation with (right panel) and without (left panel) an applied magnetic field. (b) Left panel: conduction- and valence-band relaxation after nonresonant excitation. Right panel: combined spin and recombination dynamics for nonresonant excitation.

the initialization of a resident electron spin polarization by excitation of spin-polarized electron-hole pairs is straightforward. Typically, the optically oriented holes lose their spin polarization on a very short timescale compared to the photocarrier recombination time. These depolarized holes may then recombine with electrons with arbitrary spin orientation, so that some of the electron spin polarization is transferred to the resident electrons. By contrast, in 2DHS, both, electron and hole SDT may exceed the photocarrier recombination time. Therefore, optically oriented electrons and holes will recombine according to the selection rules under emission of circularly polarized photoluminescence, and no spin polarization is transferred to the resident holes.

This process is sketched in the left panel of Fig. 2a. In order to allow for a transfer of spin polarization to the resident holes, the spin polarizations of electron and hole ensembles have to be changed during the photocarrier lifetime. Two mechanisms can be used for this: under resonant excitation conditions, an in-plane magnetic field can be applied to the sample. Due to the large difference of electron and hole  $g$  factors, the electrons precess more rapidly, and may recombine at random times during the photocarrier lifetime with holes with matching spin orientation, so that some spin-polarized holes remain after photocarrier recombination (right panel of Fig. 2a). A second mechanism is sketched in Fig. 2b. Under nonresonant excitation conditions, electron-hole pairs at finite in-plane momentum  $k$  are generated. These carriers rapidly relax to the band extrema. This momentum relaxation is typically spin-conserving for electrons, while holes lose their spin orientation during momentum relaxation. After momentum relaxation, the hole ensemble is depolarized, while there is a finite electron spin polarization. The spin-polarized electrons then recombine with holes with matching spin orientation, leaving an excess of holes with the *opposite* spin orientation.

Both of these mechanisms can be observed experimentally by TRFR and TRKR. First, we investigate magnetic-field-induced transfer of hole spin polarization. Figure 3a shows a series of TRFR traces measured on sample C at 1.2 K with different applied magnetic fields under resonant excitation conditions. We note that the trace for zero magnetic field shows a simple exponential decay with a decay constant of about 50 ps, corresponding to the photocarrier lifetime in this sample. No transfer of spin polarization to the resident holes occurs. By contrast, measurements at 3 and 6 T show, first, a damped sinusoidal oscillation, and

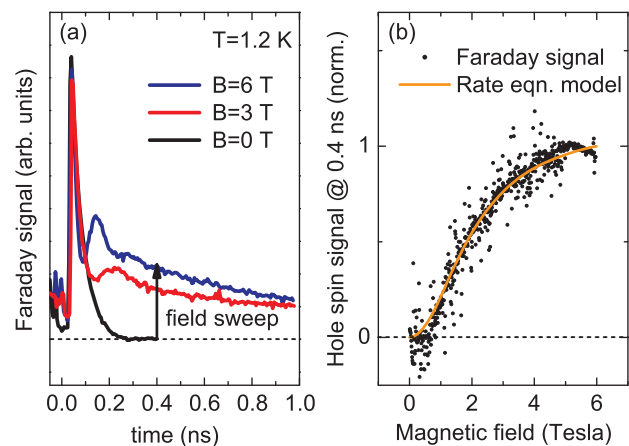


**Figure 3** (a) TRFR traces for sample C taken at 1.2 K for different magnetic fields. The arrow indicates the delay position for the magnetic field sweep shown in (b). (b) Faraday signal (black dots) as a function of magnetic field taken at a fixed time delay (400 ps) between pump and probe pulses. The orange line shows the buildup of the hole spin polarization as a function of magnetic field, as calculated by the rate equations model. Reprinted with permission from Ref. [17].

then an exponential decay with a decay constant that greatly exceeds the photocarrier lifetime. The damped oscillation stems from electron spin precession, and the long-lived exponential decay corresponds to spin dephasing of the resident holes. No hole spin precession is observed in this sample, as it has been carefully aligned with respect to the external magnetic field to minimize the hole  $g$  factor (see the discussion on hole  $g$  factor anisotropy below). We also note that the amplitude of the long-lived hole spin polarization becomes larger with higher applied magnetic field. This is investigated in more detail in the experiment shown in Fig. 3b. Here, the TRFR signal is detected at a fixed time delay between pump and probe beam (indicated by the arrow in Fig. 3a), well after photocarrier recombination is complete. The Faraday signal, which stems from the hole spin polarization, increases with the applied magnetic field and saturates at about 6 T. This indicates the magnetic-field-induced transfer of spin polarization from the optically oriented to the resident holes. We can model the combined carrier and spin dynamics of electrons and holes using a set of coupled rate equations [4, 17]:

$$\frac{d\mathbf{e}}{dt} = -\frac{\mathbf{e}}{\tau_R} + \frac{g_e\mu_B}{\hbar}(\mathbf{B} \times \mathbf{e}), \quad (2)$$

$$\frac{d\mathbf{h}}{dt} = -\frac{\mathbf{h}}{\tau_h} + \frac{g_h\mu_B}{\hbar}(\mathbf{B} \times \mathbf{h}) + \frac{e_z\mathbf{z}}{\tau_R}. \quad (3)$$

Here,  $\mathbf{e}$  and  $\mathbf{h}$  are electron and hole spin polarization vectors,  $g_e$  and  $g_h$  are the electron and hole  $g$  factors,  $\tau_R$  is the photocarrier recombination time, and  $\tau_h$  is the hole SDT. In this model, electron spin dephasing is neglected, as the electron SDT typically exceeds  $\tau_R$ . The model can quantitatively describe the measured data in Fig. 3b, as indicated by the orange line. We note that all relevant parameters, such as  $\tau_R$  and  $g_e$ , were determined in independent measurements.

We now turn to initialization of a hole spin polarization using nonresonant excitation. Figure 4a shows a series of TRKR traces measured on sample D at 15 K. In this measurement series, the laser excitation energy was increased from resonant excitation conditions to higher energies. For resonant excitation, just as discussed above, the TRKR signal consists of a simple exponential decay, indicating photocarrier recombination. As the excitation energy is increased, however, the signal shape becomes more complex: the Kerr signal rapidly decays partially, crosses the zero line, indicating an opposite spin polarization, then decays back to zero. We also note that the signal amplitude *decreases* with increasing excess energy of the excitation. This is due to the fact that the absorption of the pump beam is reduced as the laser is detuned from resonance. Additionally, the degenerate probe beam is also detuned, yielding a smaller Kerr response for a given spin polarization. These two effects limit the excess energy range, accessible in the experiment. The complex shape of the Kerr signal arises from a combination of several processes: due to the nonresonant excitation, a part of the optically oriented holes rapidly lose their spin polarization within a few picoseconds, while the electron

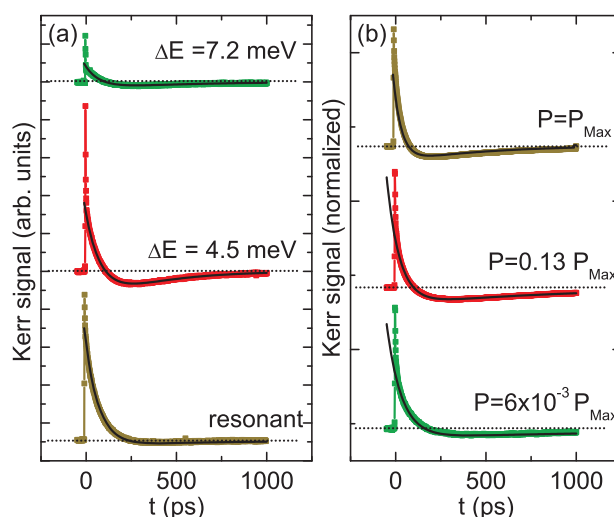


**Figure 4** (a) TRKR traces measured on sample D at 15 K with different laser excitation energies (symbols). (b) TRKR traces measured on sample D at 10 K with fixed, near-resonant laser excitation energy and various pump powers (symbols). The solid lines in both panels represent fits to the data according to the theory.

spin polarization remains constant during energy relaxation. The spin-polarized electrons then recombine with holes with matching spin orientation, so that an excess of holes with the opposite spin orientation remains, leading to the zero crossing of the Kerr signal. This indirectly generated hole spin polarization subsequently decays. These combined carrier and spin dynamics were modeled, using a Markovian master equation approach [27]. Here, the initial rapid depolarization of the optically oriented holes is considered to be instantaneous, giving an initial ratio of electron and hole spin polarizations. This model can quantitatively describe the Kerr signal in the whole time range except for the first few picoseconds, where the rapid hole dephasing occurs, as the black solid lines in Fig. 4a demonstrate. The model allows to extract, both, the initial hole/electron spin polarization ratio, and the hole SDT. For resonant excitation, this initial ratio is close to unity, while for the largest detuning values attainable in the experiment, it is reduced to about 20%. Remarkably, the hole SDT does not change significantly as a function of the excess energy.

In a second series of TRKR measurements, shown in Fig. 4b, the laser energy is kept fixed for near-resonant excitation conditions, and the pump beam power is increased by more than 2 orders of magnitude. We see that for weak, near-resonant excitation, almost no negative Kerr signal is observed, indicating no significant transfer of spin polarization to resident holes. As the pump power is increased, a pronounced zero crossing of the Kerr signal occurs. Again, the experimental curves are reproduced by the model, except for the rapid initial decay. The spin polarization ratio drops from more than 60% at weak excitation to less than 10% at high pump powers, indicating that rapid hole depolarization occurs under these excitation conditions, most likely due to

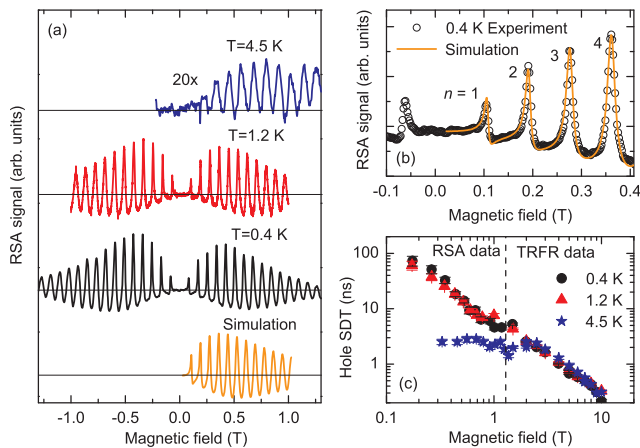


**Figure 5** (a) RSA traces for sample D, measured at different temperatures, compared to simulation data. (b) RSA trace measured at 400 mK (open circles) compared to simulation data (orange line). (c) Hole SDT, determined from RSA data (left of the dotted line) and TRFR data (right of the dotted line), for different temperatures as a function of magnetic field. Reprinted with permission from Ref. [17].

increased, non-spinconserving carrier-carrier scattering. For very large pumping powers, the hole SDT extracted from the data (not shown) decreases slightly, indicating sample heating. A detailed theoretical study of rapid hole spin dephasing, induced by phonons, was performed recently [28].

**2.4 Resonant spin amplification in two-dimensional hole systems** We now focus on resonant spin amplification measurements on 2DHS. The RSA technique, which was introduced by Kikkawa and Awschalom [29], has been successfully applied to study long-lived spin coherence in a number of systems, including n-bulk GaAs [30], QWs [26, 31], and 2DES [24]. It overcomes many of the limitations in typical TRFR/TRKR setups, in which only a small time window is accessible for time-resolved measurements. In order to extract parameters from RSA spectra, however, it is necessary to utilize a model that takes into account the peculiarities of the system under investigation, such as spin dephasing anisotropy [32],  $g$  factor inhomogeneity or carrier dynamics. We first consider RSA measurements under resonant excitation conditions. Figure 5a shows a series of RSA traces measured on sample D at different temperatures. We clearly see that there are no RSA peaks at zero magnetic field in any of the three spectra, indicating that there is no transfer of spin polarization to the resident holes at zero field under resonant excitation. As the magnetic field is increased, RSA peaks appear, and initially, their amplitude increases due to the magnetic-field induced transfer of hole spin polarization. The RSA peak amplitude then decreases again at higher applied fields due to  $g$  factor inhomogeneity. While the RSA peaks at 0.4 and 1.2 K are well-defined and narrow, the RSA trace measured at 4.5 K shows a much weaker signal and very broad peaks. As the direct comparison between measurement and a simulation,

based on the rate equation model discussed above, demonstrates (Fig. 5b), the model precisely captures all salient features of the RSA traces, including the asymmetric shape of the first RSA peak. This allows us to extract all relevant parameters, including the magnetic field dependence of the hole SDT, the hole  $g$  factor and its inhomogeneity, from the experimental data.

The hole SDT is plotted in Fig. 5c. Here, data from RSA and TRFR measurements are aggregated. The RSA measurements allow us to probe hole spin dynamics in weak magnetic fields, and we clearly observe a large increase of the hole SDT at 1.2 and 0.4 K with reduction of the magnetic field due to a suppression of the inhomogeneous broadening, with maximum values of more than 70 ns. By contrast, at liquid-helium temperatures, the hole SDT saturates at about 2.5 ns even in low magnetic fields, indicating that it is limited by another dephasing mechanism. Two processes may limit the hole SDT at low temperatures. One dephasing mechanism is based on the interaction of the hole spin with the fluctuating nuclear spins of the surrounding GaAs crystal. For localized *electrons*, this mechanism is often dominant, as the *s*-like electron wave function leads to strong contact hyperfine interaction with the nuclei. For holes, due to their *p*-like wave function, the contact hyperfine interaction is strongly suppressed. The dipolar hole–nuclei interaction remains allowed, and is about 1 order of magnitude weaker than the contact hyperfine interaction. However, it is suppressed even in the presence of small in-plane magnetic fields [33], therefore, we may neglect its effects in the RSA measurements. Another cause for hole spin dephasing is the finite admixture of LH states to the HH band for  $k \sim 0$  [34]. This small admixture gives a finite probability for hole spin dephasing during momentum scattering. Therefore, it strongly depends on the average in-plane hole momentum, and, correspondingly, on the hole gas temperature. This is in good agreement with the rapid decrease of the hole SDT with temperature, observed in the RSA experiments.

We now discuss the RSA experiments, performed under nonresonant excitation conditions or high excitation density. As described above, under these conditions, a transfer of spin polarization to the resident holes is possible even at zero magnetic field. This is clearly visible also in the RSA traces. Figure 6 shows RSA spectra measured at 1.2 K on sample D for (a) different detunings from resonance and (b) different excitation densities. As discussed above, for resonant, weak excitation, the characteristic RSA shape with no peak at zero magnetic field is observed (Fig. 6a). For nonresonant excitation, an RSA peak with negative signal amplitude appears at zero magnetic field, and as the detuning is increased (upper trace in Fig. 6a), additional negative RSA peaks are observed at finite fields. For a certain magnetic field, a node in the RSA spectrum is visible, then the RSA peak orientation flips to positive amplitudes at higher magnetic fields. For the measurement series with increasing excitation density (Fig. 6b), a similar behavior is observed in the RSA spectra. This complex signal shape indicates that the transfer of spin polarization to resident holes occurs due

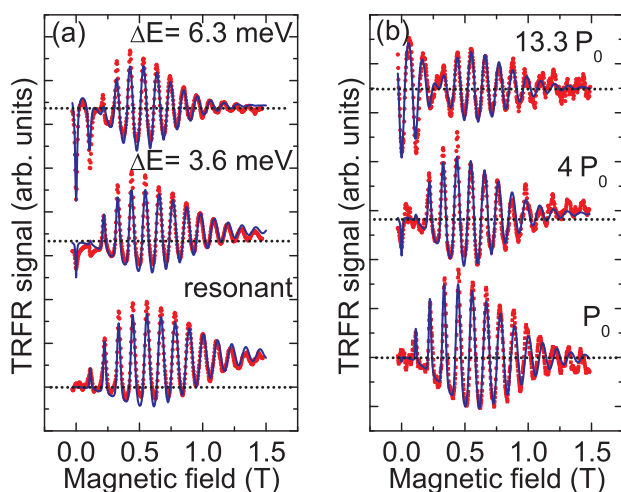


**Figure 6** Experimental RSA traces for sample D (red points) and best fits according to the theory (blue lines) for (a) selected values of the detuning (b) selected values of the excitation density.

to a mixture of the two processes described above. For low magnetic fields, the initialization via fast hole spin dephasing dominates, while at larger magnetic fields, the precession-induced transfer is more important. The shape of the spectra can be closely modeled using the Markovian master equation approach [27], as the good agreement between experimental data and simulation in Fig. 6 shows. Remarkably, rapid hole spin dephasing and long-lived hole spin polarization coexist in our samples under these excitation conditions, and the hole spin dynamics in the first few ps after optical orientation strongly influence the RSA spectra, which are measured for a pump-probe delay of about 12 ns.

### 2.5 Hole $g$ factor anisotropy and spin dynamics in tilted fields

In contrast to the electron  $g$  factor, the hole  $g$  factor in GaAs-based QWs strongly depends on the orientation of the magnetic field [21]. In (001)-grown QWs, a large anisotropy between in-plane and out-of plane  $g$  factor is expected, and for lower-symmetric growth axes, an in-plane anisotropy also occurs. Due to this large anisotropy, the hole spin quantization axis and the magnetic field axis are not colinear, if the field is tilted from the QW plane, leading to an admixture of spin relaxation and spin dephasing processes [14]. For tilted magnetic fields, an effective hole  $g$  factor  $g_h^*$ , given by the geometric sum of in-plane ( $g_{\perp}$ ) and out-of plane ( $g_{\parallel}$ )  $g$  factors, governs the hole spin dynamics:

$$g_h^* = \sqrt{g_{\perp}^2 \cos^2 \alpha + g_{\parallel}^2 \sin^2 \alpha}. \quad (4)$$

The change of the effective hole  $g$  factor is directly observable in RSA measurements, as Fig. 7 shows. Here, a series of RSA measurements with different tilt angles of the sample with respect to the magnetic field is performed. We clearly see that the spacing of the RSA maxima is visibly reduced as the tilt angle is increased. As subsequent RSA peaks correspond to

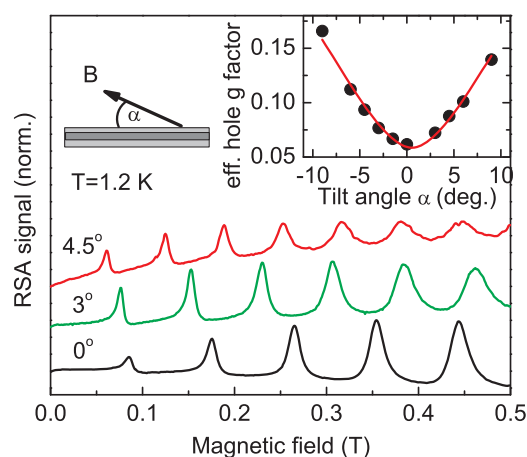


**Figure 7** RSA traces for sample D, measured at 1.2 K, for different tilt angles of the sample with respect to the external magnetic field. The inset shows the effective hole  $g$  factor determined from the spacing of the RSA maxima (black dots). Reprinted with permission from Ref. [17].

additional rotations of the hole spin polarization by  $2\pi$  during the time interval between two pump pulses, the spacing  $\Delta B$  between RSA peaks is inversely proportional to the effective hole  $g$  factor. The angle dependence of  $g_h^*$ , shown in the inset of Fig. 7, follows Eq. (4), and can be used to extract, both, the in-plane and out-of-plane hole  $g$  factors with high precision. We obtain  $|g_{\perp}| = 0.059 \pm 0.003$  and  $|g_{\parallel}| = 0.89 \pm 0.03$ .

Additionally, we observe that the RSA trace shape changes with increasing tilt angle: the RSA peak amplitude decreases, and the average Kerr signal increases with magnetic field. This change may be understood as follows: for a finite tilt angle, the optically oriented hole spin polarization can be divided into two components. A precessing component, which is perpendicular to the quantization axis, and a non-precessing component, which is parallel to it. The RSA peaks are due to constructive interference of the precessing component, which becomes smaller with increasing tilt angle. The average Kerr signal arises from constructive interference of the non-precessing component, and its amplitude is increased with the magnetic field due to the increased effectiveness of the field-induced transfer of spin polarization to the resident holes [35].

### 2.6 Electrical $g$ factor control

The  $g$  factor for electrons and holes in semiconductors strongly depends on the material. This allows for a manipulation of the  $g$  factor in QWs by use of a growth-axis electric field. The wave function of the electrons and holes is mostly confined in the QW, with a small but finite amplitude in the surrounding barriers. An electric field applied to the QW allows for a shift of the wave function towards one of the barriers, and this changes the effective  $g$  factor due to enhanced probability amplitude in the barrier material. This effect was demonstrated for electrons in a parabolic QW [36], and for holes in a p-modulation-doped QW [20]. We now turn to

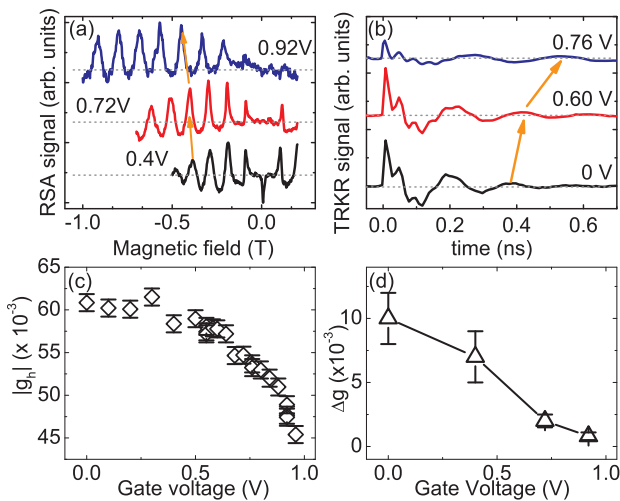


**Figure 8** (a) RSA and (b) TRKR traces for sample D with a semitransparent gate, measured at 1.2 K, for different applied gate voltages. The applied magnetic field for the TRKR traces is kept fixed at 6 T for all measurements. (c) Hole  $g$  factor and (d) hole  $g$  factor inhomogeneity as a function of gate voltage, extracted from RSA spectra.

measurements of samples, which contain a semi-transparent gate to investigate the influence of a growth-axis electric field on hole spin dynamics. Figure 8a and b shows a series of RSA and TRKR traces, measured on sample D at 1.2 K. In the RSA traces, we clearly see a change in the spacing of the RSA peaks with changing gate voltage, indicating that the hole  $g$  factor changes. This is also evident in the hole spin precession in the TRKR traces, which were measured for a fixed magnetic field. Further, we note that RSA peaks can be observed for larger magnetic field amplitudes as the gate voltage is increased. We utilized the rate equation model to extract the dependence of the spin dynamics parameters on the gate voltage. The maximum hole SDT of about 50 ns does not change with gate voltage, but the  $g$  factor shifts by more than 30%, indicating a growth-axis displacement of the hole wave function. Additionally, increasing the gate voltage also induces a reduction of the  $g$  factor inhomogeneity. This can be explained by the fact that increasing gate voltages increase the hole density inside the QW, reducing the fluctuations of the local environment of the localized holes.

**3 Valence-band spin excitations** In the last part of this work, we summarize our recent RILS experiments on hole spin excitations in strongly doped 2DHS. These experiments reveal a fingerprint of the anisotropic hole spin splitting in 2DHSs in GaAs-based QWs.

**3.1 Samples and experiment** The samples used in RILS experiments are single-side p-modulation-doped GaAs/Al<sub>0.3</sub>Ga<sub>0.7</sub>As QWs, containing 2DHSs with relatively large carrier densities. The valence-band profile of a typical sample is displayed in Fig. 9a together with the hole distribution function. All samples were grown by MBE. Their

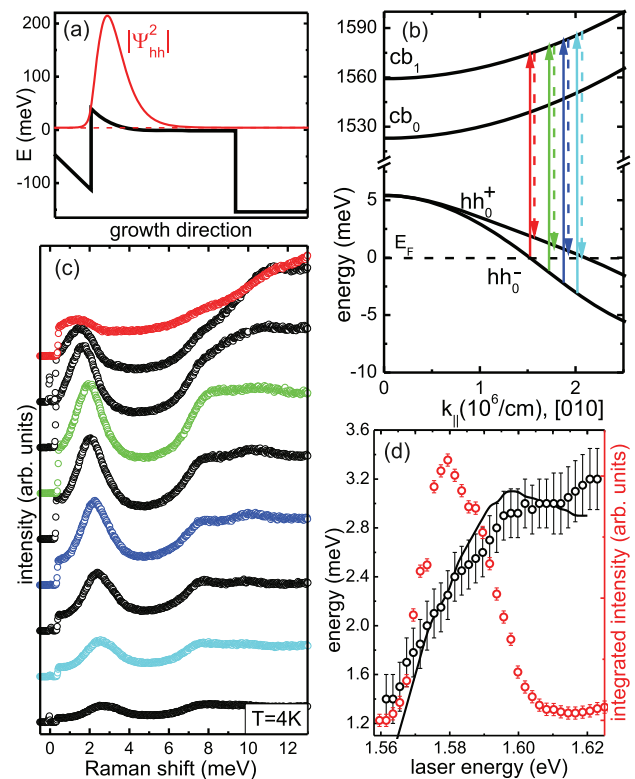


**Figure 9** (a) Valence-band potential profile calculated for sample hA. (b) Spin-split dispersion of the  $hh_0$  subband and the lowest conduction band subbands. (c) Series of depolarized  $\tilde{z}([010], [100])\tilde{z}$  RILS spectra for different laser energies from 1.567 to 1.600 eV (top to bottom spectra). Spectra are taken at nominally  $T = 4$  K, at resonance with the  $cb_1$  conduction-band subband. (d) Experimental mode positions and integrated intensities of the low-energy SDE. Reprinted with permission from Ref. [37].

properties are given in Table 2. The RILS measurements were performed in quasi-backscattering geometry, so that there is no in-plane wave vector transfer in the inelastic scattering. The samples were either mounted on the cold finger of a helium flow cryostat, or inside a bath cryostat, where they could be immersed in liquid superfluid helium. A tunable, continuous-wave Ti:sapphire laser was used for excitation. The scattered light was collected by an achromat and coupled into a triple Raman spectrometer operated in subtractive mode, so that the first two stages are used as a bandpass filter to suppress the elastically scattered light.

**Table 2** Properties of the samples used for inelastic light scattering studies. Densities and mobilities were determined from magneto-transport measurements at 4 K.

#	QW width (nm)	spacer width (nm)	hole density $p$ ( $10^{11} \text{ cm}^{-2}$ )	hole mobility $\mu$ ( $10^5 \text{ cm}^2 \text{ V}^{-1} \text{ s}^{-1}$ )
hA	20	10	9.1	0.9
hB	20	15	6.3	1.6
hC	20	20	4.7	2.0
hD	25	10	8.4	0.6

The inelastically scattered light was dispersed in the third stage of the spectrometer and detected by a liquid-nitrogen cooled charge-coupled device. All RILS spectra shown here, were collected in *depolarized* geometry, where only the light polarized perpendicular to the linearly polarized laser excitation is coupled into the spectrometer. In this scattering configuration, single-particle excitations (SPE) and SDEs are the only allowed excitations of charge carriers in resonance Raman experiments. The excitation of plasmons (charge-density excitations, CDE) is forbidden in this experimental geometry. The laser wavelength was tuned in the experiments to resonantly create electron–hole pairs with holes in the valence-band ground state and electrons in the second conduction band subband (see solid arrows in Fig. 9b). In this experimental situation, the fundamental luminescence at about 1.514 eV (not shown) is energetically well separated from the measured low-energy Raman signals and does not obscure the weak RILS spectra. For some measurement series, the crystallographic orientation of the samples relative to the polarization axis of the laser excitation was changed.

**3.2 Spin-density excitations** In the RILS experiments, an electron is resonantly excited from a state below the Fermi energy of the spin-split  $hh_0^-$  valence-band subband to the first excited conduction-band subband  $cb_1$  (see solid arrows in Fig. 9b). During the inelastic scattering process, the excited electron is instantaneously recombining with a hole in the state  $hh_0^+$  above the Fermi energy (dashed arrows in Fig. 9b). As a net effect, a  $hh_0^+ \rightarrow hh_0^-$  spinflip hole excitation is left behind in the 2DHS. Taking Coulomb interaction into account, these spinflip hole excitations form a SDE, which is a collective density oscillation of the 2DHS. From Fig. 9b, it is obvious that, by varying the laser energy, one is able to resonantly excite such hole excitations at different positions in  $k$  space, and an increase of the measured hole-excitation energy is expected with increasing laser energy. This was indeed experimentally verified [37] and can be seen in Fig. 9c and d, where measured spectra of the low-energy SDE (peak between about 1 and 3 meV in the spectra in Fig. 9c) for different laser energies and the extracted energies of the low-energy SDE are displayed, respectively. The spectra were taken in  $\bar{z}([010], [100])z$  backscattering geometry, where the incoming laser was in negative  $z$  direction, and the scattered light was detected antiparallel, in  $z$  direction. The polarization directions of linear polarizations of the laser and the scattered light were parallel to the [010] and [100] crystal directions, respectively. The solid black line in Fig. 9d gives the  $hh_0^+ - hh_0^-$  subband spacings, which were calculated, employing an eight-band  $k \cdot p$  model [37].

Figure 10a shows a comparison of RILS spectra of the low-energy SDE for samples with different hole densities, i.e., different Fermi energies in the valence band. The calculated dispersions of the spin-split hole ground states for the three samples are plotted in Fig. 10b for comparison: the increase of the Fermi energy with increasing hole density leads to a larger spinflip excitation energy, which is quantitatively confirmed in the experiments (cf. Fig. 10a).

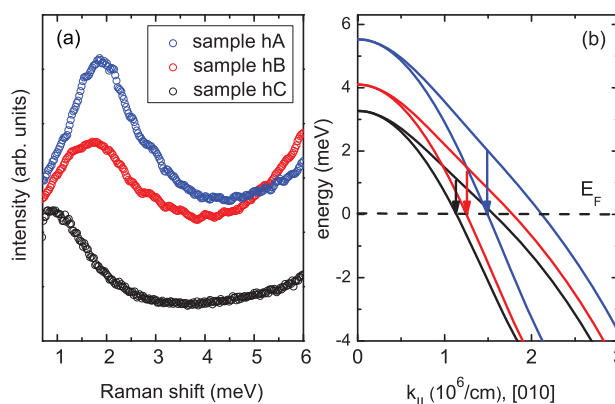


**Figure 10** (a) RILS spectra of the low-energy SDE for samples hA, hB, and hC, which all have a well width of 20 nm but different hole densities. (b) Calculated energy dispersions of the spin-split valence-band ground states of the three samples. The arrows indicate spinflip hole excitations, which may contribute to the observed low-energy SDEs.

**3.3 Valence-band spin splitting anisotropy** As mentioned above, some of the experiments were performed with different orientations of the linearly polarized laser with respect to the in-plane crystallographic axes of the QWs. It was found that [37], if the polarization direction of the laser is parallel to the [110] in-plane axis, a pronounced double-peak structure is observed in the spectra of the low-energy SDE. This can be seen in Fig. 11, where a series of spectra, taken in this scattering configuration on sample hA, is shown for different laser energies, corresponding to different positions in  $k$  space. The laser energy increases from top to bottom spectra. The double-peak structure is highlighted by black and red arrows in Fig. 11. It can be understood, if we take into account the anisotropy of the spin splitting in the  $k_x$ – $k_y$  plane. Taking into account Rashba and Dresselhaus spin–orbit coupling, this anisotropy has a twofold symmetry. Figure 12a shows the dispersions of the two lowest spin-split hole subbands, the HH and the LH subbands, for sample hA for two different in-plane directions, [010] and [110]. In the calculations, only the Rashba spin–orbit interaction was taken into account. The black and red arrows in Fig. 12a indicate the onset of spinflip hole transitions, which may contribute to the observed low-energy SDE in the experiments. One can see that there is reasonable agreement of the calculated transition energies for the two in-plane directions with the experimentally observed mode positions in Fig. 11. The continuum of excitations, which can be seen in the spectra in Fig. 11 for Raman shifts  $>7$  meV, is due to intersubband transitions of holes from the HH to the LH subbands. This can be verified by comparison of the observed excitation energies with the HH–LH spacings of the calculated subbands in Fig. 12a.

To further confirm our interpretation, that the observed double-peak structure is due to the spin-splitting anisotropy, we have calculated RILS spectra, based on the self-consistent eight-band  $k \cdot p$  bandstructure calculations [37]. Figure 12b shows a comparison of an experimental spectrum of sample

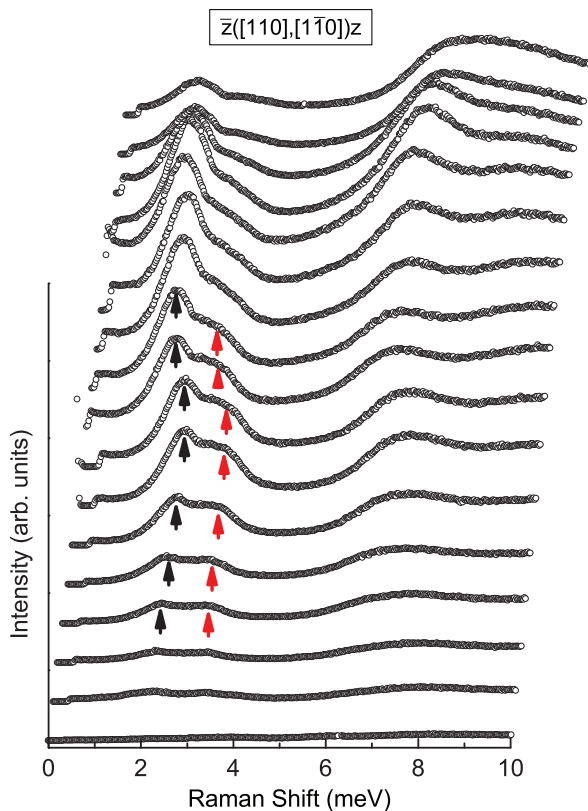


**Figure 11** Waterfall plot of depolarized  $\bar{z}([110], [1\bar{1}0])z$  RILS spectra of sample hA for different laser photon energies, which increase from top to bottom spectra from 1.567 to 1.600 eV.

hD at 1.571 eV laser energy with a simulated RILS spectrum for the same parameters. There is quite good agreement concerning mode position and line shape. However, the experimentally observed mode splitting of the double peak is about twice as large as in the simulated spectrum. It should be noted here that in the  $k \cdot p$  calculations only Rashba spin-orbit interaction was taken into account. It is likely

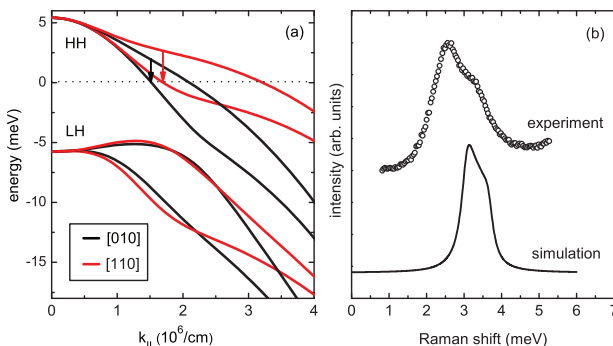


**Figure 12** (a) Energy dispersions of the spin-split HH and LH ground states for sample hA for two different in-plane directions. (b) Comparison of experimental and simulated depolarized  $\bar{z}([110], [1\bar{1}0])z$  RILS spectra of the low-energy SDE of sample hD for a laser energy of 1.571 eV.

that the neglected Dresselhaus contribution could account for the too small splitting in the simulations.

**4 Conclusions** We have investigated hole spin dynamics and hole spin excitations in GaAs-based QWs. In quantum-well samples with low hole concentrations, in the range of  $1 \times 10^{11} \text{ cm}^{-2}$  and below, we found long hole SDTs in the range of nanoseconds at low temperatures, which are due to hole localization at low temperatures. In a sample with 4 nm well width and maximum HH-LH splitting, we have observed hole SDTs above 70 ns. We have demonstrated that a spin polarization of resident holes in the samples can be optically initialized by two different mechanisms: a resonant mechanism, which requires a finite in-plane magnetic field, and, a nonresonant mechanism, which works even at zero magnetic field. Both mechanisms lead to opposite spin orientations of holes. In samples with large hole densities in the range of several  $10^{11} \text{ cm}^{-2}$ , we have directly measured the spin splitting of the hole ground state at the Fermi level via RILS on a low-energy SDE. The spectral shape of the SDE is a fingerprint of the anisotropic spin splitting of the holes in the  $k_x$ - $k_y$  QW plane.

**Acknowledgements** The authors would like to thank all those who contributed to the original publications summarized in this feature article. Financial support by the DFG via SPP 1285 and SFB 689 is gratefully acknowledged.

## References

- [1] D. Awschalom, D. Loss, and N. Samarth, *Semiconductor Spintronics and Quantum Computation* (Springer, Berlin/Heidelberg/New York, 2002).
- [2] J. Fabian, A. Matos-Abiague, C. Ertler, P. Stano, and I. Zutic, *Acta Phys. Slov.* **57**, 565 (2007).
- [3] M. W. Wu, J. H. Jiang, and M. Q. Weng, *Phys. Rep.* **493**, 61–236 (2010).
- [4] T. Korn, *Phys. Rep.* **494**, 415–445 (2010).
- [5] C. Gerl, S. Schmult, U. Wurstbauer, H. Tranitz, C. Mitzkus, and W. Wegscheider, *Physica E* **32**(1–2), 258 (2006).
- [6] C. Schindler and P. Vogl, *J. Phys.: Conf. Ser.* **193**, 012103 (2009).
- [7] D. J. Hilton and C. L. Tang, *Phys. Rev. Lett.* **89**(14), 146601 (2002).
- [8] T. C. Damen, L. Via, J. E. Cunningham, J. Shah, and L. J. Sham, *Phys. Rev. Lett.* **67**(24), 3432 (1991).
- [9] B. Baylac, T. Amand, X. Marie, B. Dareys, M. Brousseau, G. Bacquet, and V. Thierry-Mieg, *Solid State Commun.* **93**, 57 (1995).
- [10] X. Marie, T. Amand, P. Le Jeune, M. Paillard, P. Renucci, L. E. Golub, V. D. Dymnikov, and E. L. Ivchenko, *Phys. Rev. B* **60**(8), 5811 (1999).
- [11] M. Syperek, D. R. Yakovlev, A. Grelich, J. Misiewicz, M. Bayer, D. Reuter, and A. D. Wieck, *Phys. Rev. Lett.* **99**(18), 187401 (2007).
- [12] J. P. Eisenstein, H. L. Störmer, V. Narayanamurti, A. C. Goswami, and W. Wiegmann, *Phys. Rev. Lett.* **53**, 2579–2582 (1984).
- [13] B. Jusserand, D. Richards, H. Peric, and B. Etienne, *Phys. Rev. Lett.* **69**(5), 848 (1992).

- [14] P. Machnikowski and T. Kuhn, *Phys. Rev. B* **81**(11), 115306 (2010).
- [15] I. A. Yugova, M. M. Glazov, E. L. Ivchenko, and A. L. Efros, *Phys. Rev. B* **80**(10), 104436 (2009).
- [16] Y. El Khalifi, B. Gil, H. Mathieu, T. Fukunaga, and H. Nakashima, *Phys. Rev. B* **39**(18), 13533 (1989).
- [17] T. Korn, M. Kugler, M. Griesbeck, R. Schulz, A. Wagner, M. Hirmer, C. Gerl, D. Schuh, W. Wegscheider, and C. Schüller, *New J. Phys.* **12**, 043003 (2010).
- [18] M. J. Snelling, G. P. Flinn, A. S. Plaut, R. T. Harley, A. C. Tropper, R. Eccleston, and C. C. Phillips, *Phys. Rev. B* **44**(20), 11345 (1991).
- [19] I. A. Yugova, A. Greilich, D. R. Yakovlev, A. A. Kiselev, M. Bayer, V. V. Petrov, Y. K. Dolgikh, D. Reuter, and A. D. Wieck, *Phys. Rev. B* **75**(24), 245302 (2007).
- [20] M. Kugler, T. Andlauer, T. Korn, A. Wagner, S. Fehrer, R. Schulz, M. Kubová, C. Gerl, D. Schuh, W. Wegscheider, P. Vogl, and C. Schüller, *Phys. Rev. B* **80**(3), 035325 (2009).
- [21] R. Winkler, S. J. Papadakis, E. P. De Poortere, and M. Shayegan, *Phys. Rev. Lett.* **85**(21), 4574 (2000).
- [22] A. Zrenner, L. V. Butov, M. Hagn, G. Abstreiter, G. Böhm, and G. Weimann, *Phys. Rev. Lett.* **72**, 3382–3385 (1994).
- [23] D. Gammon, E. S. Snow, B. V. Shanabrook, D. S. Katzer, and D. Park, *Phys. Rev. Lett.* **76**, 3005–3008 (1996).
- [24] M. Griesbeck, M. M. Glazov, E. Y. Sherman, D. Schuh, W. Wegscheider, C. Schüller, and T. Korn, *Phys. Rev. B* **85**, 085313 (2012).
- [25] S. Varwig, A. René, A. Greilich, D. R. Yakovlev, D. Reuter, A. D. Wieck, and M. Bayer, *Phys. Rev. B* **87**, 115307 (2013).
- [26] D. R. Yakovlev and M. Bayer, *Spin Physics in Semiconductors* (Springer, Berlin, 2008), Chap. 6: Coherent spin dynamics of carriers, p. 135.
- [27] M. Kugler, K. Korzekwa, P. Machnikowski, C. Gradl, S. Furthmeier, M. Griesbeck, M. Hirmer, D. Schuh, W. Wegscheider, T. Kuhn, C. Schüller, and T. Korn, *Phys. Rev. B* **84**, 085327 (2011).
- [28] M. Gawelczyk and P. Machnikowski, *Phys. Rev. B* **87**, 195315 (2013).
- [29] J. M. Kikkawa and D. D. Awschalom, *Phys. Rev. Lett.* **80**(19), 4313 (1998).
- [30] J. Kikkawa and D. Awschalom, *Nature* **397**(6715), 139 (1999).
- [31] I. A. Yugova, A. A. Sokolova, D. R. Yakovlev, A. Greilich, D. Reuter, A. D. Wieck, and M. Bayer, *Phys. Rev. Lett.* **102**(16), 167402 (2009).
- [32] M. M. Glazov and E. L. Ivchenko, *Semiconductors* **42**(8), 951 (2008).
- [33] J. Fischer, W. A. Coish, D. V. Bulaev, and D. Loss, *Phys. Rev. B* **78**(15), 155329 (2008).
- [34] J. W. Luo, G. Bester, and A. Zunger, *Phys. Rev. B* **79**(12), 125329 (2009).
- [35] K. Korzekwa, C. Gradl, M. Kugler, S. Furthmeier, M. Griesbeck, M. Hirmer, D. Schuh, W. Wegscheider, T. Kuhn, C. Schüller, T. Korn, and P. Machnikowski, *Phys. Rev. B* **88**, 155303 (2013).
- [36] G. Salis, Y. Kato, K. Ensslin, D. C. Driscoll, A. C. Gossard, and D. D. Awschalom, *Nature* **414**, 619 (2001).
- [37] M. Hirmer, M. Hirmer, D. Schuh, W. Wegscheider, T. Korn, R. Winkler, and C. Schüller, *Phys. Rev. Lett.* **107**, 216805 (2011).